REPORTS

PEROVSKITE LEDS

Overcoming the electroluminescence efficiency limitations of perovskite light-emitting diodes

Himchan Cho,[1]* Su-Hun Jeong,[1]* Min-Ho Park,[1]* Young-Hoon Kim,[1] Christoph Wolf,[1] Chang-Lyoul Lee,[2] Jin Hyuck Heo,[3] Aditya Sadhanala,[4] NoSoung Myoung,[2] Seunghyup Yoo,[5] Sang Hyuk Im,[3] Richard H. Friend,[4] Tae-Woo Lee[1,6]†

Organic-inorganic hybrid perovskites are emerging low-cost emitters with very high color purity, but their low luminescent efficiency is a critical drawback. We boosted the current efficiency (CE) of perovskite light-emitting diodes with a simple bilayer structure to 42.9 candela per ampere, similar to the CE of phosphorescent organic light-emitting diodes, with two modifications: We prevented the formation of metallic lead (Pb) atoms that cause strong exciton quenching through a small increase in methylammonium bromide (MABr) molar proportion, and we spatially confined the exciton in uniform $MAPbBr_3$ nanograins (average diameter = 99.7 nanometers) formed by a nanocrystal pinning process and concomitant reduction of exciton diffusion length to 67 nanometers. These changes caused substantial increases in steady-state photoluminescence intensity and efficiency of $MAPbBr_3$ nanograin layers.

Organic-inorganic hybrid perovskites (OIPs) have recently been established as an important class of materials in photovoltaic devices, and there has been rapid progress in increasing their power conversion efficiency (*1*–*5*). OIPs are emerging also as promising light emitters because they can provide very high color purity (full width at half maximum ~ 20 nm) irrespective of the crystal size, unlike conventional inorganic quantum dots, because their intrinsic crystal structure is similar to a multiple quantum well (*6*, *7*). Also, OIPs have low material cost and a simply tunable band gap, with a reasonable ionization energy (IE) comparable to that of common hole-injection materials (*7*–*11*). Thus, OIPs are attractive materials as alternative emitters that can overcome the disadvantages of organic light-emitting diodes (OLEDs) (e.g., complex synthesis, high cost, and poor color purity) and inorganic quantum dot LEDs (e.g., complex synthesis, high cost, and high IE).

Bright electroluminescence (EL) (>100 cd m^{-2}) at room temperature from perovskite light-emitting diodes (PeLEDs) with a methylammonium lead halide ($MAPbX_3$, where X is I, Br, or Cl) emission layer was demonstrated recently (*6*, *7*, *12*–*18*). As an emission layer, $MAPbBr_3$ has higher air stability (*7*, *19*) and exciton binding energy (76 or 150 meV) than does $MAPbI_3$ (30 or 50 meV) (*20*, *21*). However, PeLEDs have much lower current efficiency (CE) at room temperature than do OLEDs or quantum dot LEDs. Existing methods have not overcome the substantial luminescence quenching in $MAPbX_3$ caused by facile thermal ionization of excitons generated in the OIP layer, which has a low exciton binding energy. Spin-coating of $MAPbBr_3$ solution creates a rough, nonuniform surface with many cuboids of large grain size (*22*), which leads to a substantial leakage current and large exciton diffusion length, L_D, that reduces CE in PeLEDs. To improve the CE of PeLEDs, the OIP grain size must be decreased, and OIP films should be flat and uniform. Smaller grains can spatially limit the L_D of excitons or charge carriers and reduce the possibility of exciton dissociation into carriers. This fabrication goal differs from that of the OIP layers in solar cells, which should be dense films with large grain size to achieve facile exciton diffusion and dissociation. Thus, processes designed to achieve uniform OIP film morphology with large grain size in solar cells, such as solvent engineering (*23*, *24*), are not applicable to PeLEDs, which require a small L_D.

Here, we report a systematic approach for achieving highly bright and efficient green PeLEDs with CE = 42.9 cd A^{-1} and external quantum efficiency (EQE) = 8.53%, even in a simplified bilayer structure. These high efficiencies represent a >20,000-fold increase compared with that of the control devices and are higher than the best EQEs of a previous report regarding visible PeLEDs using OIP films by factors of >10.6 (table S1 and fig. S1) (*15*). The high-efficiency PeLEDs were constructed on the basis of effective management of exciton quenching by a modified $MAPbBr_3$ emission layer that was achieved with (i) fine and controllable stoichiometry modification and (ii) optimized nanograin engineering by nanocrystal pinning (NCP) (fig. S2). Furthermore, we demonstrated a flexible PeLED using a self-organized conducting polymer (SOCP) anode and the first large-area PeLED (2 cm by 2 cm pixel).

A fundamental problem that must be solved to achieve high CE in PeLEDs is minimizing the presence of metallic Pb atoms in $MAPbBr_3$ that limits the efficiency of PeLEDs. Metallic Pb atoms can emerge in $MAPbBr_3$ even if MABr and $PbBr_2$ are mixed in 1:1 (mol:mol) ratios because of the unintended losses of Br atoms or incomplete reaction between MABr and $PbBr_2$ (*25*). Excess Pb atoms degrade luminescence by increasing the nonradiative decay rate and decreasing the radiative decay rate (*26*). Preventing the formation of metallic Pb atoms was achieved by finely increasing the molar proportion of MABr by 2 to 7% in $MAPbBr_3$ solution (fig. S2A). Use of excess MABr suppressed exciton quenching and reduced the hole-injection barrier from SOCP layers (table S2) to $MAPbBr_3$ layers with decreased IE and greatly increased the steady-state photoluminescence (PL) intensity and PL lifetime of $MAPbBr_3$ films. We propose that the PL process in $MAPbBr_3$ nanograins depends on trap-assisted recombination at grain boundaries and radiative recombination inside the grains. Second, the CE in PeLEDs can be increased by decreasing $MAPbBr_3$ grain sizes, which improves uniformity and coverage of $MAPbBr_3$ nanograin layers and radiative recombination by confining the excitons in the nanograins (leading to small L_D). An optimized NCP process (fig. S3) helped to change the morphology of $MAPbBr_3$ layers from scattered micrometer-sized cuboids to well-packed nanograins with uniform coverage, which greatly reduced leakage current and increased CE.

We fabricated $MAPbBr_3$ films by spin-coating with stoichiometrically modified perovskite solutions on prepared glass/SOCPs or silicon wafer/SOCPs substrates later used in devices (Fig. 1, A and B), and then characterized the films' morphologies and optoelectronic properties. The solutions had different molar ratios of MABr to $PbBr_2$ (MABr:$PbBr_2$ = 1.05:1, 1:1, or 1:1.05). To achieve uniform surface coverage and reduced grain size, we used NCP instead of normal spin coating (fig. S3). This process washed out the "good" solvents [dimethylformamide or dimethyl sulfoxide (DMSO)] and causes pinning of NCs by inducing fast crystallization. Chloroform was

[1]Department of Materials Science and Engineering, Pohang University of Science and Technology (POSTECH), 77 Cheongam-Ro, Pohang, Gyungbuk 790-784, Republic of Korea. [2]Advanced Photonics Research Institute (APRI), Gwangju Institute of Science and Technology (GIST), 1 Oryong-dong, Buk-gu, Gwangju 500-712, Republic of Korea. [3]Department of Chemical Engineering, College of Engineering, Kyung Hee University, 1 Seochon-dong, Giheung-gu, Youngin-si, Gyeonggi-do 446-701, Republic of Korea. [4]Cavendish Laboratory, University of Cambridge, J J Thomson Avenue, Cambridge CB3 0HE, UK. [5]Department of Electrical Engineering, Korea Advanced Institute of Science and Technology (KAIST), 373-1 Guseong-dong, Yuseong-gu, Daejeon 305-701, Republic of Korea. [6]Department of Chemical Engineering, Division of Advanced Materials Science, School of Environmental Science and Engineering, Pohang University of Science and Technology (POSTECH), 77 Cheongam-Ro, Nam-Gu, Pohang, Gyungbuk 790-784, Republic of Korea.
*These authors contributed equally to this work. †Corresponding author. E-mail: twlee@postech.ac.kr, taewlees@gmail.com

chosen as the solvent for NCP because a highly volatile nonpolar solvent is suitable to reduce the size and increase the uniformity of $MAPbBr_3$ grains by reducing solvent evaporation time. In addition, to further reduce grain size, we devised additive-based NCP (A-NCP), which uses an organic small molecule, 2,2′,2″-(1,3,5-benzinetriyl)-tris (1-phenyl-1-H-benzimidazole) (TPBI), as an additive to chloroform, whereas pure chloroform is used in solvent-based NCP (S-NCP).

The use of NCP affected film morphology (Fig. 2). Without NCP, micrometer-sized $MAPbBr_3$ cuboids were scattered on the SOCP layer (Fig. 2A). They were only interconnected with a few other cuboids, so a large amount of space remained uncovered. This high surface roughness and the formation of pinholes in OIP films result in formation of a bad interface with the electron transport layer and electrical shunt paths, and thus severely limit CE in PeLEDs. In contrast, when NCP was used, perfect surface coverage was obtained, and the $MAPbBr_3$ crystal morphology changed to a well-packed assembly of tiny grains ranging from 100 to 250 nm (Fig. 2, B to E, and fig. S4). $MAPbBr_3$ grain size was very slightly affected by the stoichiometric modification of $MAPbBr_3$ solutions (Fig. 2, B to D, and fig. S4, A to C). Furthermore, $MAPbBr_3$ grain size was greatly reduced to 50 to 150 nm (average = 99.7 nm) by A-NCP (Fig. 2E and fig. S4D). This reduction can be attributed to hindrance of crystal growth by TPBI molecules during crystal pinning. The thickness of $MAPbBr_3$ layer was ~400 nm (Fig. 1B).

The crystal structures of $MAPbBr_3$ films were analyzed by measuring x-ray diffraction (XRD) patterns (Fig. 2F, fig. S5, and table S3). The XRD patterns of $MAPbBr_3$ films (1:1) exhibit peaks at 15.02°, 21.3°, 30.28°, 33.92°, 37.24°, 43.28°, and 46.00° that can be assigned to (100), (110), (200), (210), (211), (220), and (300) planes, respectively, by using Bragg's law to convert the peak positions to interplanar spacings (Fig. 2F). The lattice parameter is in accordance with a previous report (*19*) and demonstrates that $MAPbBr_3$ films had a stable cubic $Pm\bar{3}m$ phase. Using the Scherrer equation, we calculated the crystallite size to be 24.4 ± 2.4 nm, and the variation with stoichiometric change was not large (table S3). Because the crystallite sizes were much smaller than the apparent grain sizes (Fig. 2, A to E), we conclude that all grains consisted of many crystallites. The stoichiometric changes had very little effect on the peak positions (fig. S5A). Furthermore, A-NCP did not change the peak positions when compared to S-NCP (fig. S5); this stability in positions indicates that the stoichiometric changes of $MAPbBr_3$ solution and the use of TPBI additive did not affect the crystal structure of $MAPbBr_3$ films.

To study chemical changes in the $MAPbBr_3$ layers fabricated with perovskite solutions of different stoichiometries, we conducted x-ray photoelectron spectroscopy (XPS). The survey spectra showed strong peaks of Br (~68 eV), Pb (~138 and 143 eV), C (~285 eV), and N (~413 eV); these results agree with values in previous reports (fig. S6A) (*7*, *25*, *27*, *28*). Systematic deconvolution of Pb4f, Br3d, and N1s spectra into summations of Gaussian-Lorentzian curves revealed the nature of chemical bonds in $MAPbBr_3$ (figs. S6, B to D, and S7). We confirmed the gradual increase in MABr molar proportion in the films by observing the gradual increase in N1s peak intensities as $MABr:PbBr_2$ increased from 1:1.05 to 1.05:1 (fig. S7, C and D) and the gradual decrease in Br:Pb atomic ratio (supplementary text F). In the Pb4f spectra (fig. S6, B to F), large peaks were observed at ~138.8 and ~143.6 eV (caused by the spin orbit split) that correspond to $Pb4f_{7/2}$ and $Pb4f_{5/2}$ levels, respectively (*25*, *27*, *28*). Each of these peaks was associated with a smaller peak that was shifted to 1.8-eV lower binding energy; these small peaks can be assigned to metallic Pb (*25*, *27*, *28*). The height of peaks that represent metallic Pb decreased as $MABr:PbBr_2$ increased from 1:1.05 to 1:1 (fig. S6, E and F); this peak was absent in the film with $MABr:PbBr_2$ = 1.05:1 (fig. S6F). This trend indicates that the presence of metallic Pb atoms on the films was successfully prevented by fine stoichiometry control. In contrast, the high peak intensity of the metallic Pb peak in the films with $MABr:PbBr_2$ = 1:1 and 1:1.05 suggests that numerous

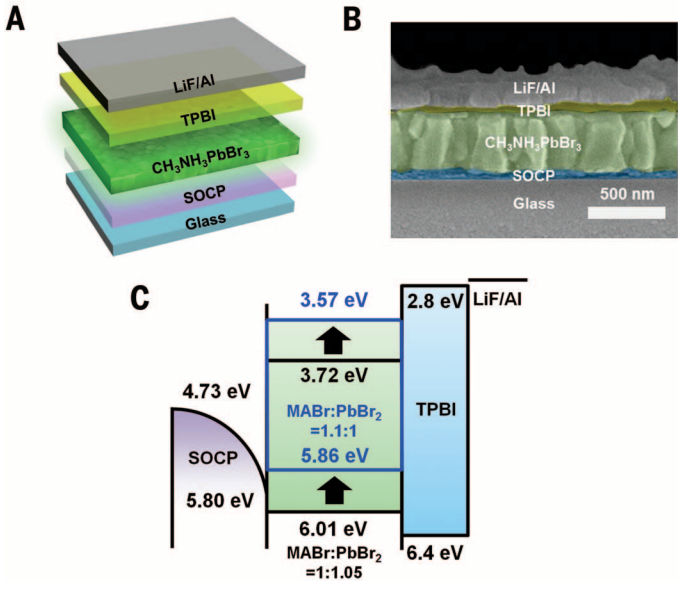

Fig. 1. Schematic illustrations of device structure and its cross-sectional scanning electron microscope (SEM) image, and energy band structure. (**A**) The device structure. (**B**) Cross-sectional SEM image of PeLEDs. (**C**) Energy band diagram of PeLEDs, showing a decrease in IE with increasing MABr molar proportion.

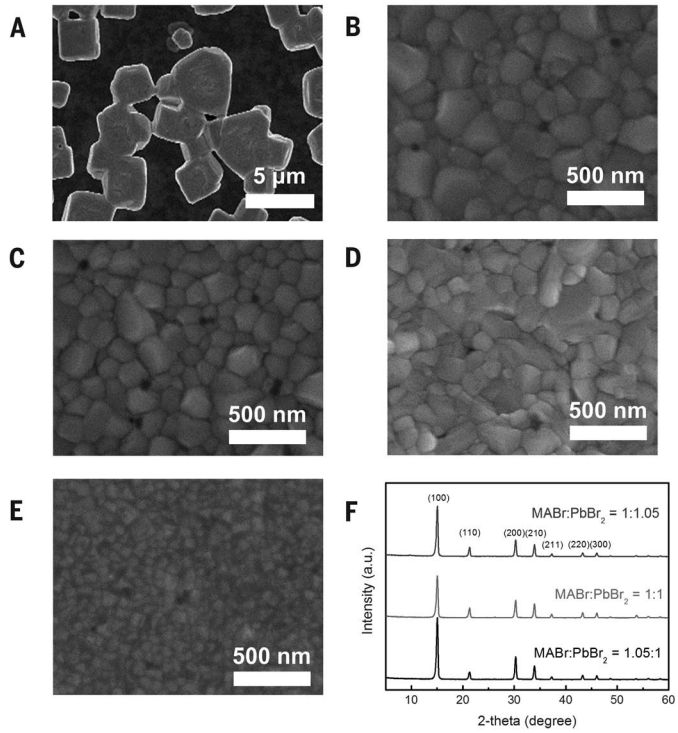

Fig. 2. SEM images and XRD patterns of $MAPbBr_3$ layers. SEM images of $MAPbBr_3$ layers of (**A**) $MABr:PbBr_2$ = 1:1 without NCP, (**B**) 1:1.05, (**C**) 1:1, (**D**) 1.05:1 with S-NCP, and (**E**) 1.05:1 with A-NCP. (**F**) XRD patterns of $MAPbBr_3$ nanograin layers with $MABr:PbBr_2$ = 1:1.05, 1:1, and 1.05:1.

metallic Pb atoms were formed on the film surfaces.

We measured the work functions (WFs) and IEs of the $MAPbBr_3$ films using ultraviolet photoelectron spectroscopy (UPS) (fig. S8). The WFs were obtained by subtracting the energies at secondary cut-offs of the UPS spectra from the ultraviolet radiation energy of 21.2 eV when a Fermi level of 0 eV was the common reference for all energies. The IEs were determined by adding the WF (fig. S8A) to the energy offset between WFs and IEs of $MAPbBr_3$ (fig. S8B) (*29*). The IE gradually decreased with increasing MABr molar proportion from 6.01 eV in the film with MABr:$PbBr_2$ = 1:1.05 to 5.86 eV in the film with MABr:$PbBr_2$ = 1.1:1 (Fig. 1C and table S4).

Table 1. Maximum CE of PeLEDs depending on NCP and the molar ratio of MABr:$PbBr_2$.

MABr:$PbBr_2$	NCP type	Max. CE (cd A^{-1})
1.05:1	A-NCP	42.9
1.07:1	S-NCP	19.3
1.05:1	S-NCP	21.4
1.03:1	S-NCP	4.03
1.02:1	S-NCP	0.457
1:1	S-NCP	0.183
1:1.05	S-NCP	4.87×10^{-2}
1:1	Without NCP	2.03×10^{-3}

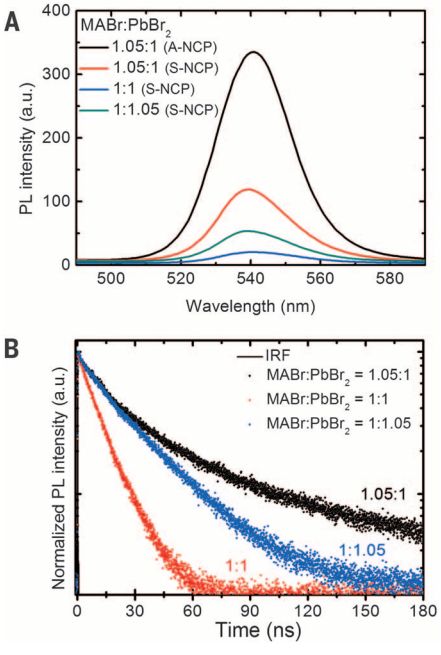

Fig. 3. Steady-state PL spectra and lifetime. (**A**) Steady-state PL spectra of $MAPbBr_3$ nanograin layers with NCP type and varying molar ratio of MABr:$PbBr_2$. (**B**) PL lifetime curves of $MAPbBr_3$ nanograin layers with varying molar ratio of MABr:$PbBr_2$. Black line: instrument response function (IRF).

The gradual decrease in IEs with decreasing $PbBr_2$ molar proportion can be understood on the basis of the IE being greater in $PbBr_2$ than in $MAPbBr_3$ (*30*). In PeLEDs, this decrease can help alleviate hole-injection barriers from SOCP layers to $MAPbBr_3$ layers (Fig. 1C).

The luminescent properties of the $MAPbBr_3$ films were investigated by steady-state PL measurement (Fig. 3A). We carried out the measurement using a spectrofluorometer with excitation from monochromatic light with a wavelength of 405 nm (xenon lamp). The $MAPbBr_3$ films fabricated from MABr:$PbBr_2$ = 1.05:1 had a ~ 5.8 times increase in PL intensity (Fig. 3A) compared with 1:1 films and had much higher PL quantum efficiency (PLQE; 36% versus 3%). In addition, the reduction in grain size with A-NCP versus S-NCP increased the PL intensity by ~2.8 times. The PL intensity of the films with MABr:$PbBr_2$ = 1:1.05 was greater than in those with MABr:$PbBr_2$ = 1:1, although the $PbBr_2$ molar proportion had increased in the former. We suspect that this departure from the expected trend is due to $PbBr_2$-induced surface passivation of the film, which reduces nonradiative recombination at the trap sites (*31*).

To understand the kinetics of excitons and free carriers in $MAPbBr_3$ films and how the presence of metallic Pb atoms affects the PL lifetime, we conducted time-correlated single-photon counting measurements (Fig. 3B). The PL decay curves were fitted with a bi-exponential decay model, in which the PL lifetime is considered as the summation of fast- and slow-decay components that give a short lifetime τ_1 and a long lifetime τ_2, respectively. To investigate the quality of quenching sites, we prepared the layers (MABr:$PbBr_2$ = 1.05:1) with and without sealing with a 50-nm-thick poly(methyl methacrylate) (PMMA) layer. The fraction f_2 of τ_2 decreased from 91 to 77% in the film without sealing (table S5). Oxygen and moisture can diffuse quickly into grain boundaries when the top

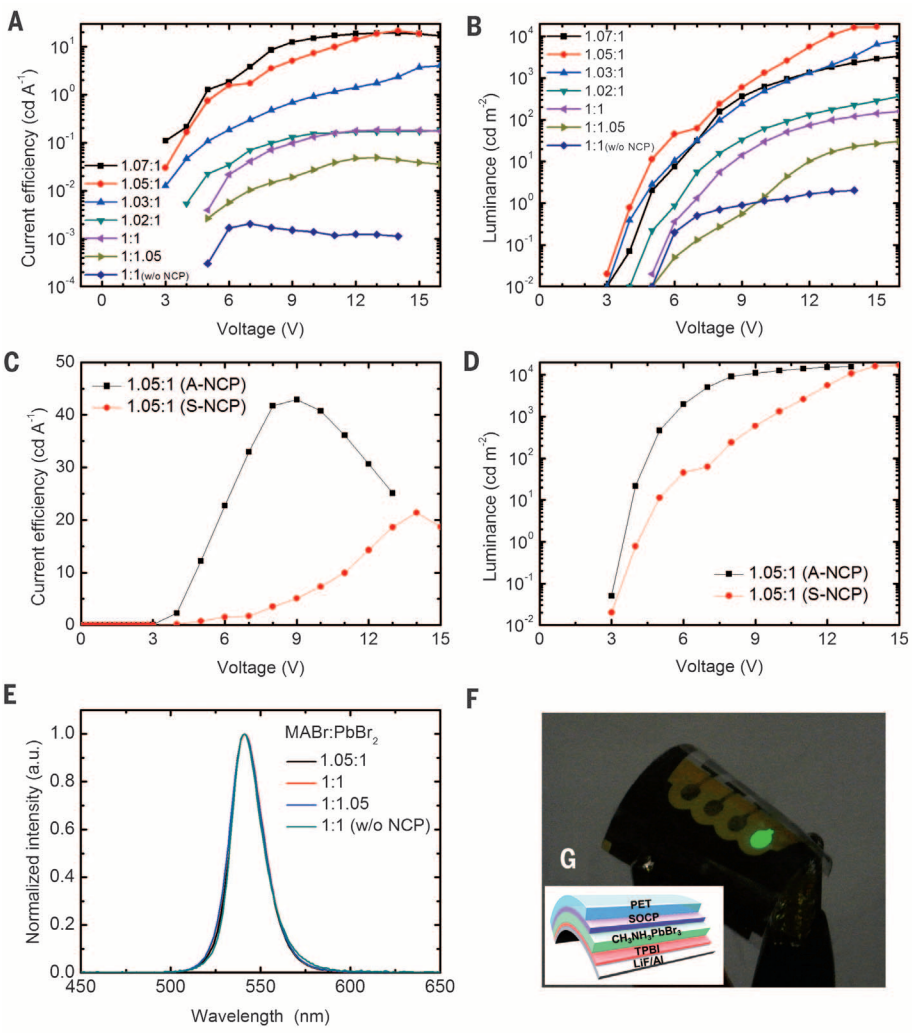

Fig. 4. PeLED characteristics, EL spectra, and photograph of PeLED. (**A** and **B**) CE and luminance of PeLEDs based on S-NCP and $MAPbBr_3$ nanograin emission layers with varying molar ratio of MABr:$PbBr_2$ (■ 1.07:1, ● 1.05:1, ▲1.03:1, ▼1.02:1, ◀1:1, ▶1:1.05, ◆1:1 without NCP). (**C** and **D**) CE and luminance of PeLEDs based on A-NCP and $MAPbBr_3$ nanograin emission layers. (**E**) EL spectra of PeLEDs. (**F**) Photograph of a flexible PeLED, and (**G**) its device structure.

PMMA layer is not used; oxygen or moisture at grain boundaries provides quenching sites. The fast decay is related to trap-assisted recombination at grain boundaries, whereas the slow decay is related to radiative recombination inside the grains (fig. S9) (*32*).

This proposition was supported by analyzing the change in τ and f of $MAPbBr_3$ films with varying stoichiometric ratio. As $MABr:PbBr_2$ increased from 1:1 to 1.05:1, the average lifetime τ_{avg} gradually increased from 12.2 to 51.0 ns (table S5). The short τ_{avg} (12.2 ns) in the film with $MABr:PbBr_2$ = 1:1 originated from the substantial reduction in τ_2. This implies that uncoordinated metallic Pb atoms at grain boundaries inhibit radiative recombination and cause strong nonradiative recombination (fig. S9). The $MAPbBr_3$ films fabricated with $PbBr_2$-rich perovskite solution ($MABr:PbBr_2$ = 1:1.05) had a longer lifetime than films with $MABr:PbBr_2$ = 1:1, possibly through $PbBr_2$-induced surface passivation (*31*). We calculated the average L_D using a model similar to that in a previous report (fig. S10) (*33*). The films ($MABr:PbBr_2$ = 1.05:1) underneath a PMMA layer exhibited a much smaller L_D (67 nm) than those previously reported (>1 μm) (*34*). We attribute this reduction in L_D to the reduced grain sizes in which excitons are under stronger spatial confinement, thereby reducing dissociation and enhancing radiative recombination; this compensates the plausible adverse effect of larger grain boundary area (*6*).

The PeLED fabricated from the $MAPbBr_3$ solution ($MABr:PbBr_2$ = 1:1) without using NCP showed poor luminous characteristics (maximum CE = 2.03 × 10^{-3} cd A^{-1}), mainly owing to high leakage current (fig. S11). In contrast, maximum CE was substantially increased (0.183 cd A^{-1}) when a full-coverage uniform $MAPbBr_3$ nanograin layer ($MABr:PbBr_2$ = 1:1) with decreased grain size was achieved with S-NCP, without stoichiometric modifications to avoid metallic Pb atoms (Fig. 4, A and B, and Table 1). The maximum CE was boosted to 21.4 cd A^{-1} in the PeLEDs fabricated with perovskite solutions with excess MABr (1.07:1, 1.05:1, 1.03:1 and 1.02:1) (Fig. 4A and Table 1). As $MABr:PbBr_2$ increased from 1:1 to 1.05:1, the maximum CE varied from 0.183 to 21.4 cd A^{-1}.

We further increased the CE of PeLEDs by using A-NCP. The PeLEDs based on A-NCP had a maximum CE of 42.9 cd A^{-1} (Fig. 4, C and D, and Table 1), which represents an EQE of 8.53% when the angular emission profile is considered (fig. S12). The EL spectra of PeLEDs were very narrow; full width at half maximum was ~20 nm for all spectra. This high color purity of OIP emitters shows great potential when used in displays (Fig. 4E). A pixel of the PeLED based on $MABr:PbBr_2$ = 1.05:1 exhibited strong green-light emission (fig. S13A). Furthermore, the proposed processes and materials used therein are compatible with flexible and large-area devices; a high-brightness flexible PeLED (Fig. 4, F and G) and a large-area (2 cm by 2 cm pixel) PeLED (fig. S13B) were fabricated. Our study reduces the technical gap between PeLEDs and OLEDs or quantum dot LEDs and is a big step toward the development of efficient next-generation emitters with high color purity and low fabrication cost based on perovskites.

REFERENCES AND NOTES

1. W. S. Yang *et al.*, *Science* **348**, 1234–1237 (2015).
2. M. Liu, M. B. Johnston, H. J. Snaith, *Nature* **501**, 395–398 (2013).
3. N. J. Jeon *et al.*, *Nature* **517**, 476–480 (2015).
4. J.-H. Im, I.-H. Jang, N. Pellet, M. Grätzel, N.-G. Park, *Nat. Nanotechnol.* **9**, 927–932 (2014).
5. H. Kim, K.-G. Lim, T.-W. Lee, *Energy Environ. Sci.* 10.1039/c5ee02194d (2015)
6. Z.-K. Tan *et al.*, *Nat. Nanotechnol.* **9**, 687–692 (2014).
7. Y.-H. Kim *et al.*, *Adv. Mater.* **27**, 1248–1254 (2015).
8. D. B. Mitzi, *Chem. Mater.* **8**, 791–800 (1996).
9. M. R. Filip, G. E. Eperon, H. J. Snaith, F. Giustino, *Nat. Commun.* **5**, 5757 (2014).
10. T. M. Koh *et al.*, *J. Phys. Chem. C* **118**, 16458–16462 (2014).
11. G. E. Eperon *et al.*, *Energy Environ. Sci.* **7**, 982–988 (2014).
12. R. L. Z. Hoye *et al.*, *Adv. Mater.* **27**, 1414–1419 (2015).
13. N. K. Kumawat, A. Dey, K. L. Narasimhan, D. Kabra, *ACS Photonics* **2**, 349–354 (2015).
14. G. Li *et al.*, *Nano Lett.* **15**, 2640–2644 (2015).
15. J. Wang *et al.*, *Adv. Mater.* **27**, 2311–2316 (2015).
16. A. Sadhanala *et al.*, *Adv. Electron. Mater.* **1**, 1500008 (2015).
17. J. C. Yu *et al.*, *Adv. Mater.* **27**, 3492–3500 (2015).
18. N. K. Kumawat *et al.*, *ACS Appl. Mater. Interfaces* **7**, 13119–13124 (2015).
19. J. H. Noh, S. H. Im, J. H. Heo, T. N. Mandal, S. I. Seok, *Nano Lett.* **13**, 1764–1769 (2013).
20. I. B. Koutselas, L. Ducasse, G. C. Papavassiliou, *J. Phys. Condens. Matter* **8**, 1217–1227 (1996).
21. K. Tanaka *et al.*, *Solid State Commun.* **127**, 619–623 (2003).
22. J. H. Heo, D. H. Song, S. H. Im, *Adv. Mater.* **26**, 8179–8183 (2014).
23. Z. Xiao *et al.*, *Adv. Mater.* **26**, 6503–6509 (2014).
24. N. J. Jeon *et al.*, *Nat. Mater.* **13**, 897–903 (2014).
25. R. Lindblad *et al.*, *J. Phys. Chem. C* **119**, 1818–1825 (2015).
26. E. Dulkeith *et al.*, *Nano Lett.* **5**, 585–589 (2005).
27. S. Gonzalez-Carrero, R. E. Galian, J. Pérez-Prieto, *J. Mater. Chem. A* **3**, 9187–9193 (2015).
28. I. A. Shkrob, T. W. Marin, *J. Phys. Chem. Lett.* **5**, 1066–1071 (2014).
29. P. Schulz *et al.*, *Energy Environ. Sci.* **7**, 1377–1381 (2014).
30. J. Kanbe, H. Onuki, R. Onaka, *J. Phys. Soc. Jpn.* **43**, 1280–1285 (1977).
31. Q. Chen *et al.*, *Nano Lett.* **14**, 4158–4163 (2014).
32. D. Shi *et al.*, *Science* **347**, 519–522 (2015).
33. S. D. Stranks *et al.*, *Science* **342**, 341–344 (2013).
34. R. Sheng *et al.*, *J. Phys. Chem. C* **119**, 3545–3549 (2015).

ACKNOWLEDGMENTS

This work was partially supported by Samsung Research Funding Center of Samsung Electronics under Project Number SRFC-MA-1402-07. A.S. was partially supported by the Engineering and Physical Sciences Research Council (UK). All data are available in the main text and the supplementary materials.

SUPPLEMENTARY MATERIALS

www.sciencemag.org/content/350/6265/1222/suppl/DC1
Materials and Methods
Supplementary Text
Figs. S1 to S13
Tables S1 to S5
References (*35*–*43*)

4 August 2015; accepted 22 October 2015
10.1126/science.aad1818

LASER PHYSICS

Ultraviolet surprise: Efficient soft x-ray high-harmonic generation in multiply ionized plasmas

Dimitar Popmintchev,[1] Carlos Hernández-García,[1,2] Franklin Dollar,[1] Christopher Mancuso,[1] Jose A. Pérez-Hernández,[3] Ming-Chang Chen,[4] Amelia Hankla,[1] Xiaohui Gao,[5] Bonggu Shim,[5] Alexander L. Gaeta,[5] Maryam Tarazkar,[6] Dmitri A. Romanov,[7] Robert J. Levis,[6] Jim A. Gaffney,[8] Mark Foord,[8] Stephen B. Libby,[8] Agnieszka Jaron-Becker,[1] Andreas Becker,[1] Luis Plaja,[2] Margaret M. Murnane,[1] Henry C. Kapteyn,[1] Tenio Popmintchev[1]*

High-harmonic generation is a universal response of matter to strong femtosecond laser fields, coherently upconverting light to much shorter wavelengths. Optimizing the conversion of laser light into soft x-rays typically demands a trade-off between two competing factors. Because of reduced quantum diffusion of the radiating electron wave function, the emission from each species is highest when a short-wavelength ultraviolet driving laser is used. However, phase matching—the constructive addition of x-ray waves from a large number of atoms—favors longer-wavelength mid-infrared lasers. We identified a regime of high-harmonic generation driven by 40-cycle ultraviolet lasers in waveguides that can generate bright beams in the soft x-ray region of the spectrum, up to photon energies of 280 electron volts. Surprisingly, the high ultraviolet refractive indices of both neutral atoms and ions enabled effective phase matching, even in a multiply ionized plasma. We observed harmonics with very narrow linewidths, while calculations show that the x-rays emerge as nearly time-bandwidth–limited pulse trains of ~100 attoseconds.

High-order harmonic generation (HHG) results from the extreme quantum nonlinear response of atoms to intense laser fields: Atoms in the process of being ionized by an intense femtosecond laser pulse coherently emit short-wavelength light that can extend well into the soft x-ray region (*1*–*6*). When implemented in a phase-matched geometry to ensure that the laser and HHG fields both propagate at the same speed ~*c*, HHG from

Overcoming the electroluminescence efficiency limitations of perovskite light-emitting diodes

Himchan Cho *et al.*

Science **350**, 1222 (2015);
DOI: 10.1126/science.aad1818